Influence of Mn on Mechanical Properties and Hardening Behaviors of High Carbon Containing Austenitic Manganese Fe-*x*Mn-2Cr-1.3C Steels

Kulsiri Pothikamjorn* and Phacharaphon Tunthawiroon
Department of Industrial Engineering, Faculty of Engineering, King Mongkut's Institute of Technology Ladkrabang, Bangkok 10520, Thailand
***Corresponding author E-mail:** kulsirikwang@gmail.com
Received: April 1, 2020 **Revised:** June 15, 2020 **Accepted:** June 18, 2020

Abstract

The mechanical properties and hardening behaviors of the high carbon containing Fe-13Mn, Fe-18Mn, and Fe-20Mn steels was investigated in this study. The microstructures of the experimental steels were researched using the electron back-scattered diffraction, EBSD and X-ray diffraction, XRD techniques. The mechanical properties of the steels were characterized by hardness and monotonic tensile tests. The hardening behavior was determined based on the material constants obtained from the relationship between the true stress and true strain. The results indicated that the Mn concentrations were insignificantly affected on the microstructure and the phase of Fe-*x*Mn steels, as well as the hardness and tensile properties. The power law relation during the plastic deformation for Fe-13Mn, Fe-18Mn, and Fe-20Mn steels could be predicted to be $\sigma = 2230.62\varepsilon^{0.474}$, $\sigma = 2240.41\varepsilon^{0.433}$, and $\sigma = 2051.64\varepsilon^{0.381}$, respectively. The strength coefficient, K and the strain hardening exponent, n, were found to be decreased with increasing Mn concentrations. Reduction of the strain hardening exponent led to the decline in strain hardening rate ($d\sigma/d\varepsilon$) during the plastic deformation of Fe-*x*Mn steels.

Keywords: Fe-Mn steels, mechanical property, tensile tests, hardening behavior, strain hardening rate

1. Introduction

Manganese steels, also call Austenitic Manganese steels or Mangalloys or Hadfield steels have been extensively used for many industrial fields owing to their good toughness and high ductility [1], [2]. A notable property of manganese steels is high work hardening capacity and high resistant to abrasion, compared to the other carbon steels [3]. Moreover, manganese steels are non-magnetic because they are characterized by a fully austenitic microstructure even at the room temperature [4]–[7]. Thus, this kind of steels is suitable for the heavy industrial fields, such as mining, railroad industry, cement industry and etc., [2], [3], [8]–[10]. For the commercial manganese steels, the manganese concentrations are incorporated between 3 and 12 wt.% with a small amount of carbon ranging from 0.2 to 1.0 wt.% [11], [12]. Both manganese and carbon are responsible for solid-solution strengthening and precipitation strengthening effects in the steels as well as austenite stabilizer. Addition of the additive elements, such as Cr, Mo and Ti are much more effective in aforementioned strengthening effects [13]–[15]. However, adding the extra elements is an optional to raise the cost of steels to have more specific mechanical properties.

Recently, the manganese steels are considered as the prospective alloys for using in the automotive industry[6], [15]–[17]. Moreover, the development of these steels is being carried out in order to obtain the satisfaction and/or suitable performance for each service. This development leads to emerge the various manganese steel compositions. They could be basically categorized to be low, medium and high manganese steels based on the level of manganese concentrations. Generally, low manganese steels contain the manganese contents at about 3-12 wt.%. For the medium and high manganese steels, the extra manganese concentrations are typically added between 15 and 30 wt.% [14]. Based on the literature [8], the high manganese steels (HMS) with high strength have been intentionally developed since 2011. Many studies attempted to enhance the mechanical properties of HMS with heat treatments and the second-phase precipitations [3], [15]. Nonetheless, the existing researches focusing on the work hardening behavior of HSM are limited even though it is a crucial property of this steel composition. Therefore, in this research, the hardening behaviors of the high manganese steels (the Mn concentrations are between 13 and 20 wt.%) are studied via the room temperature tensile testing.

2. Experiments

2.1. Materials

The high carbon containing Fe-*x*Mn steels (supplied by Sammitr Metal Works Co.,Ltd., Thailand) were used in this study, where x is the Mn concentrations varying between 13, 18, and 20 wt.%. The high purity of elements was melted in electrical furnace and then casted into round bars with a dimeter of approximate 25 mm and length of 300 mm using the sand mold. The as-cast steels were subjected to the homogenizing heat treatment at 1250 ºC for 6 h, followed by air cooling. Subsequently, the homogenized steels were heat-treated at 1050 ºC for 6 h, followed by quenching in water. The heat treatment profile used to prepare the experimental Fe-*x*Mn steels was illustrated in Fig. 1. The chemical compositions of the as-cast Fe-*x*Mn steels, individually examined using optical emission spectroscopy, OES, are tabulated in Table 1. Hereafter, the experimental steels are labeled as Fe-13Mn, Fe-18Mn, and Fe-20Mn based on the Mn concentrations used in this study.

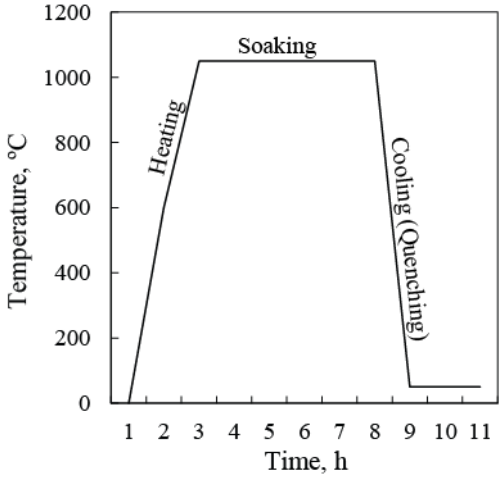

Fig. 1. Heat treatment profile used to prepare the experimental Fe-*x*Mn steels

Table 1. Chemical compositions of the experimental steels used in this study

Elements (wt.%)	Experimental steels		
	Fe-13Mn	Fe-18Mn	Fe-20Mn
Mn	13.20	17.80	19.40
Cr	2.00	1.90	2.05
C	1.27	1.31	1.33
Si	0.45	0.54	0.58
Ni	<0.1	<0.1	<0.1
P	<0.04	<0.04	<0.04
S	<0.03	<0.03	<0.03
Fe	Bal.	Bal.	Bal.

2.2. Microstructure observation

The initial microstructure was examined using the electron back-scattered diffraction, EBSD, equipped with scanning electron microscope, SEM. The primary electron beam, which typically has an energy of 20 keV was applied during EBSD analysis. In order to confirm the phases of experimental steels, X-ray diffraction, XRD was carried out. X-ray diffraction patterns were obtained with a diffractometer using a Cu Kα (0.1547 nm) radiation source. The applied voltage and current were 40 mA and 45 kV. During the XRD measurements, each steel was scanned from 30º to 120º (2θ) with the step size of 1º/min.

2.3. Mechanical property and hardening behavior characterization

The mechanical properties of the experimental Fe-*x*Mn steels were characterized on the basis of hardness and uniaxial tensile tests conducted at the room temperature. The hardness was carried out using the micro Vickers hardness method. The indentation load and duration for each measurement were 1000 g and 15 s, respectively. For the uniaxial tensile test, the tensile specimens were prepared in accordance with the American Standard for Testing Materials (ASTM) E8M. The dimensions for tensile specimen were illustrateed in Fig. 2. The specimen was individually strained with a constant strain rate of $1.5\text{x}10^{-4}$ s^{-1} corresponding to the travelling speed of 0.1 mm/min. The hardening behavior was evaluated in the term of the strain hardening rate expressed by the following equation:

$$\frac{d\sigma}{d\varepsilon} = n\frac{\sigma}{\varepsilon} \tag{1}$$

where n is the strain hardening exponent, σ is the true stress and ε is the true strain.

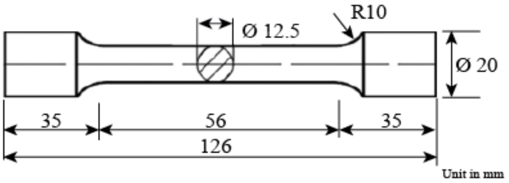

Fig. 2. Geometry of tensile specimen prepared in accordance with ASTM: E8M

3. Results and discussion

3.1. Microstructure

The microstructure of the experimental Fe-*x*Mn steels was analyzed by EBSD technique as shown in Fig. 3–5. Figure 3a–c illustrate the EBSD inverse pole figure (IPF) maps of the Fe-13Mn, Fe-18Mn, and Fe-20Mn steels. According to EBSD analysis, an equiaxed-grain structure was observed in the experimental steels with a large grain size ranging from a few hundred micrometer to few millimeters. The IPF maps (Fig. 3) reveal that the crystalline orientation of Fe-*x*Mn steels were randomly distributed as the colors were varied. In the other words, the experimental steels exhibited a lack of preferred orientation of crystalline grain formed during the fabrication and preparation, consistent with [17]. Thus, influence of steels microstructure on the mechanical properties and hardening behaviors could be neglected. The image quality (IQ) maps together with boundary rotation angle of Fe-13Mn, Fe-18Mn, and Fe-20Mn steels were depicted in Fig. 4a–c. Based on the IQ maps, the grain boundaries of steels were clearly revealed. In addition, for all experimental steels, the most inclination angle of the grain boundary was observed to be higher than 15^{o} (represented by the blue line along the grain boundaries in IQ maps) suggesting the high angle misorientation structure. Figure 5a–c, respectively show the phase maps of the Fe-13Mn, Fe-18Mn, and Fe-20Mn. According to the equilibrium phase diagram of the Fe-Mn system [18] and the cooling (quenching) method used in this research, the phases, including ferrite (α) and austenite (γ) as well as martensitic structure, should coexist theoretically. Therefore, in the EBSD phase mapping analysis, the above-mentioned phases were chosen as database for evaluation and analysis. However, the phase of the experimental Fe-*x*Mn steels was a fully austenite (γ) structure as the monocolor (only green color) was revealed in the EBSD phase maps. The presence of a single austenitic phase was attributed to the influence of Mn which extended the austenitic (γ) field in the iron-carbon phase diagram [18]. To assure the phase of Fe–*x*Mn steels, XRD analysis was conducted and the XRD patterns are shown in Fig. 6. The several peaks associated with an austenitic structure were indicated without the presence of other and carbide phases although the experimental steels contained the high concentrations of carbon.

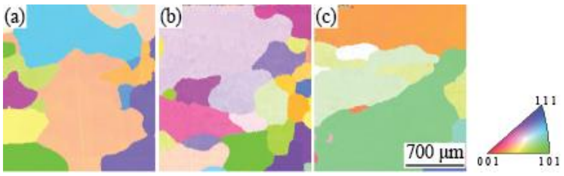

Fig. 3. EBSD inverse pole figure (IPF) map of (a) Fe-13Mn, (b) Fe-18Mn, and (c) Fe-20Mn

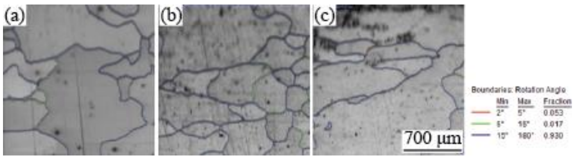

Fig. 4. EBSD image quality (IQ) map of (a) Fe-13Mn, (b) Fe-18Mn, and (c) Fe-20Mn

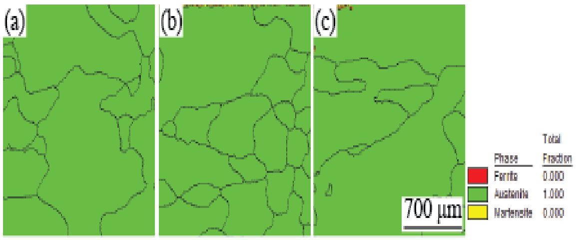

Fig. 5. EBSD phase map of (a) Fe-13Mn, (b) Fe-18Mn, and (c) Fe-20Mn

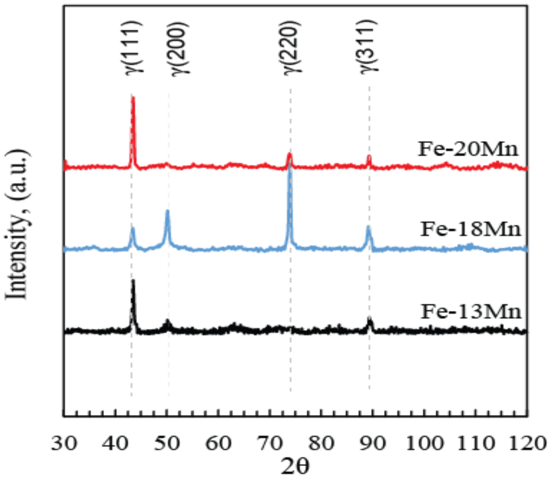

Fig. 6. XRD pattern of Fe–13Mn, Fe–18Mn, and Fe–20Mn steels

3.2. Mechanical properties

Figure 7 compares the hardness of the experimental Fe-*x*Mn steels after the heat treatment process. The average hardness of the Fe–13Mn, Fe–18Mn, and Fe–20Mn steels was 233.01 ± 3.2, 232.90 ± 3.7, and 231.72 ± 4.6 HV, respectively. The fundamental tensile properties of Fe-*x*Mn steels, including yield stress, tensile strength, and elongation determined from the tensile tests, were summarized in Table 2. The yield stress, tensile strength, and elongation were accordingly varied between 450-480 MPa, 720-780 MPa, and 32-38%. Both hardness and tensile results indicated that Fe-13Mn, Fe-18Mn, and Fe-20Mn exhibited the similar mechanical properties [12]. Thus, it would be deduced that the concentrations of Mn between 13 and 20 (wt.%) did not influence on the hardness and tensile properties of the high carbon Fe-*x*Mn steels.

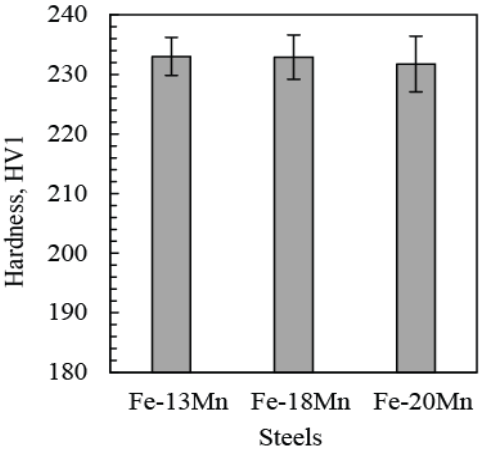

Fig. 7. Hardness of experimental steels

Table 2. The tensile properties obtained from the tensile tests

	Yield stress (MPa)	Tensile strength (MPa)	Elongation (%)
Fe-13Mn	481.41 ± 25.0	786.34 ± 86.4	39.73 ± 5.3
Fe-18Mn	480.07 ± 36.5	784.01 ± 26.4	39.92 ± 5.6
Fe-20Mn	452.38 ± 38.2	720.17 ± 66.4	32.50 ± 12.8

3.3. Strain hardening behavior of Fe-*x*Mn

To obtain the hardening parameters during the plastic deformation of the tensioned Fe-*x*Mn specimens, the engineering stress and engineering strain obtained from the tensile testing were transformed to the true stress and true strain by the following equations:

$$\sigma = s(e + 1) \tag{2}$$

$$\varepsilon = \ln(e + 1) \tag{3}$$

where σ is the true stress and ε is the true strain. The engineering stress and engineering strain are denoted as s and e. Figure 8 illustrates the representative true stress-strain curves of the experimental Fe-*x*Mn steels. The results indicated that the relation between true stress and true strain for Fe-13Mn, Fe-18Mn, and Fe-20Mn steels were almost the same. The curves display the deformation behavior in both the elastic and plastic regions obviously. According to the true stress-strain curves in Fig. 8, the elastic region which is characterized by a proportional relationship between stress and strain was found in the true strain between 0 and 0.07 whereas the plastic region presented when the true strain was greater than 0.07 until the rupture strain. The deformation behavior in the plastic region could express by the simple power law relation as follows:

$$\sigma = K\varepsilon^{n} \qquad (4)$$

where K is the strength coefficient and n is the strain hardening exponent. A log-log plot of the true stress and true strain curves of Fe-*x*Mn steels, shown in Fig. 9, results in transformation of power law relation to linear relation. Based on the power law relation, eq. (4), the value of K and n for Fe-13Mn, Fe-18Mn, and Fe-20Mn steels could be predicted to be $\sigma = 2230.62\varepsilon^{0.474}$, $\sigma = 2240.41\varepsilon^{0.433}$, and $\sigma = 2051.64\varepsilon^{0.381}$, respectively. The K and n value of the experimental steels were compared as dipicted in Fig. 10. By comparison, the K and n were slightly decreased as the Mn concentrations increased. Generally, the value of n is normally used to determine the ability to raise the hardness and strength of materials during the plastic deformation. Therefore, according to the obtained results, the higher Mn concentrations, low ability to raise the hardness, effectively enhance the resistance to plastic flow during the deformation of the high carbon containing Fe-*x*Mn steels.

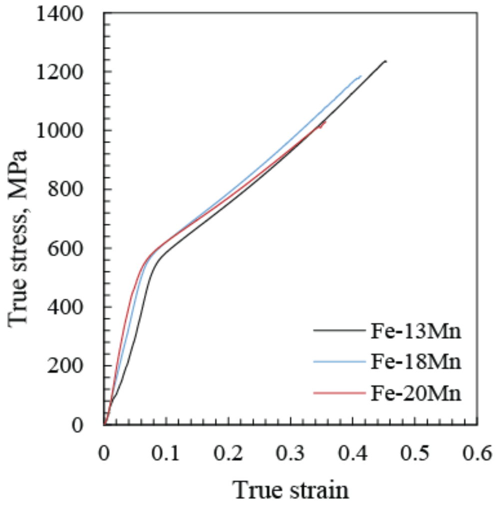

Fig. 8. True stress-stain of experimental steels

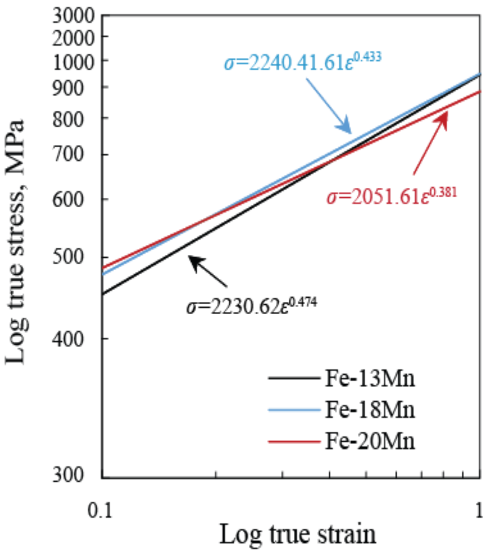

Fig. 9. Logarithmic representative of true stress-strain curve with hardening exponent, *n* and strength coefficient, *K*

Figure 11 compares the strain hardening rate ($d\sigma/d\varepsilon$) together with the true stress-strain curves of the experimental Fe-*x*Mn steels. Given that the strain hardening rate is not identical with the strain hardening exponent, *n*. It is generally used to explain the work hardening behavior which depends on the state of strain [1], [9], [19], [20]. From the strain hardening rates plotted in Fig. 11, behavior of strain hardening for the experimental Fe-*x*Mn steels could be clearly divided into two stages depending on the strain level. In the small strain level or the initial plastic deformation corresponding to the true strain between 0.1-0.2, the hardening rate value was rapidly decreased. The decrease in this value might attribute to the ready movement of deformation slip. In contrast, the strain hardening rate value was slowed down in the higher plastic deformation portion or higher strain level. As the deformation level increased, the dislocation density as well as mechanical twinning area became higher, contributing to the restriction of other dislocations. By comparison, the higher Mn-containing Fe-*x*Mn steels show the lower strain hardening rate ($d\sigma/d\varepsilon$) in both small and large strain level. According to literatures, [21], [22], high addition of Mn introduced the higher stacking fault (SFE) energy to the Fe-Mn steels. When the SFE is high, the materials are able to deform easily either by dislocation glide or cross slip. On the other hand, in the low SFE steels, the mobility of dislocations and cross slip would be decreased. Therefore, based on the recent study, the higher Mn in the Fe-*x*Mn steels would allow the movement of dislocation and cross slip, resulting to the lower rate of hardening and strengthening.

Since the Fe-Mn steels, usually used under the severe loading conditions, the low hardening rate is preferable because they would be damaged slowly or would have the higher capacity to absorb the energy events in service. However, higher additions of Mn would raise the cost of production of these steels.

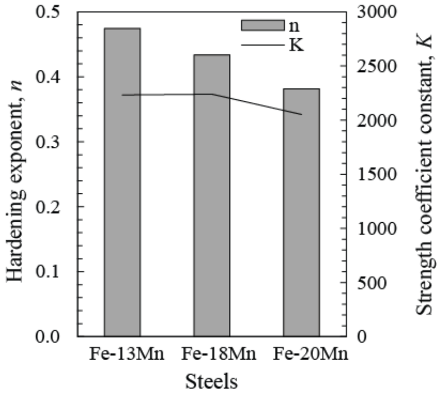

Fig. 10. Comparison of hardening exponent, *n* and strength coefficient, *K*

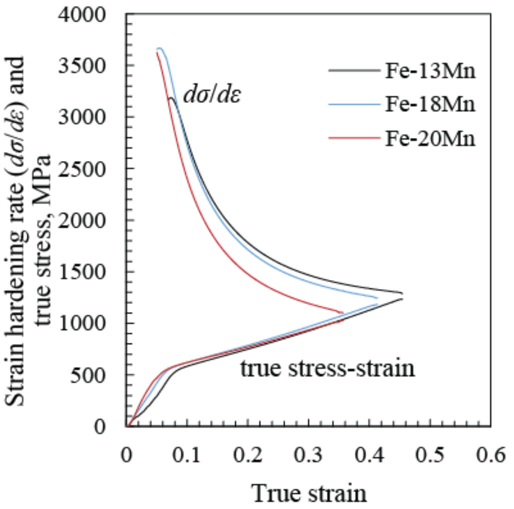

Fig. 11. Strain hardening rate ($d\sigma/d\varepsilon$) of experimental steels plotted with the true stress-strain curves

4. Conclusions

In this study, the influence of Mn concentrations on the mechanical properties and the hardening behavior of the high carbon containing Fe-*x*Mn steels was investigated. The concentrations of Mn between 13 and 20 wt% did not affect on the microstructure of Fe-*x*Mn steels. The microstructure of Fe-13Mn, Fe-18Mn, and Fe-20Mn steels exhibited a large equiaxed crystalline structure with high angle misorientation boundaries. The phase of experimental steels presented in the entire austenite (γ). The hardness and tensile properties of Fe-*x*Mn steels were minimally changed as the concentrations of Mn were varied. However, the strength coefficient, *K* and strain hardening exponent, *n* of the Fe-*x*Mn steels were slightly decreased with increasing Mn concentrations, leading to the reduction of the strain hardening rate.

5. Acknowledgements

The authors would like to thanks the Sammitr Metal Works Co.,Ltd., Thailand for supporting the experimental materials. The authors appreciatively acknowledge Prof.Chiba Akihiko and Assoc.Prof.Kenta Yamanaka of the Institute for Materials Research (IMR), Tohoku University, Japan, for contributing to the EBSD analysis.

6. References

[1] Y. H. Wen, H. B. Peng, H. T. Si, R. L. Xiong and D. Raabe, “A novel high manganese austenitic steel with higher work hardening capacity and much lower impact deformation than Hadfield manganese steel,” Materials and Design, Vol. 55, pp. 798–804, 2014.

[2] E. Bayraktar, F. A. Khalid and C. Levaillant, “Deformation and fracture behaviour of high manganese austenitic steel,” Journal of Materials Processing Technology, Vol. 147, No. 2, pp. 145–154, 2004.

[3] D. Xiaodong, S. Guodong, W. Yifei, W. Jianfeng and Y. Haoyu, “Abrasion behavior of high manganese steel under low impact energy and corrosive conditions,” Advances in Tribology, Vol. 2009, pp. 1–6, 2009.

[4] J. T. Zhang, Y. guang Zhao, J. Tan, and X. F. Xu, “Austenite Grain Refinement by Reverse α’ → γ Transformation in Metastable Austenitic Manganese Steel,” Journal of Iron and Steel Research International, Vol. 22, No. 2. pp. 157–162, 2015.

[5] J. Chen, M. yang Lv, Z. yu Liu and G. dong Wang, “Combination of ductility and toughness by the design of fine ferrite/tempered martensite-austenite microstructure in a low carbon medium manganese alloyed steel plate,” Materials Science and Engineering A, Vol. 648, pp. 51–56, 2015.

[6] Y. Zou et al., “Austenite stability and its effect on the toughness of a high strength ultra-low carbon medium manganese steel plate,” Materials Science and Engineering A, Vol. 675, pp. 153–163, 2016.

[7] A. K. Chandan, G. K. Bansal, J. Kundu, J. Chakraborty and S. G. Chowdhury, “Effect of prior austenite grain size on the evolution of microstructure and mechanical properties of an intercritically annealed medium manganese steel,” Materials Science and Engineering A, Vol. 768, No. August, p. 138458, 2019.

[8] W. Bleck, “High Manganese Steel 2016,” Steel Research International, Vol. 89, No. 9, p. 1800390, 2018.

[9] A. Grajcar, A. Kozłowska and B. Grzegorczyk, “Strain hardening behavior and microstructure evolution of high-manganese steel subjected to interrupted tensile tests,” Metals, Vol. 8, No. 2, 2018.

[10] W. S. Owen and M. Grujicic, “Strain aging of austenitic hadfield manganese steel,” Acta Materialia, Vol. 47, No. 1, pp. 111–126, 1998.

[11] B. Hu, B. Bin He, G. J. Cheng, H. W. Yen, M. X. Huang and H. W. Luo, “Super-high-strength and formable medium Mn steel manufactured by warm rolling process,” Acta Materialia, Vol. 174, pp. 131–141, 2019.

[12] B. Sun et al., “Microstructural characteristics and tensile behavior of medium manganese steels with different manganese additions,” Materials Science and Engineering A, Vol. 729, No. April, pp. 496–507, 2018.

[13] R. P. Dalai, S. Das and K. Das, “Development ofTiCreinforced austenitic manganese steel,” Canadian Metallurgical Quarterly, Vol. 53, No. 3, pp. 317–325, 2014.

[14] F. Kies et al., “Design of high-manganese steels for additive manufacturing applications with energy-absorption functionality,” Materials and Design, Vol. 160, pp. 1250–1264, 2018.

[15] A. Grajcar, A.Kozłowska, and B. Grzegorczyk, “Microstructure evolution and phase composition of high-manganese austenitic steels,” Journal of Achievements in Materials and Manufacturing Engineering, Vol. 31, No. 2, pp. 218–225, 2008.

[16] B. Gumus et al., “Twinning activities in high-Mn austenitic steels under high-velocity compressive loading,” Materials Science and Engineering A, Vol. 648, pp. 104–112, 2015.

[17] S. I. Lee, S. Y. Lee, J. Han, and B. Hwang, Deformation behavior and tensile properties of an austenitic Fe-24Mn-4Cr-0.5C high-manganese steel: Effect of grain size, Vol. 742. Elsevier B.V., 2019.

[18] W. Huang, “An Assessment of the Co-Mn System,” Calphad, Vol. 13, No. 3, pp. 231–242, 1989.

[19] K. S. Raghavan, M. Sastri and M. J. Marcinkowski, “Nature of Work-Hardening Behavior in Hadfield’S Manganese Steel,” Met Soc of AIME-Trans, Vol. 245, No. 7, pp. 1569–1575, 1969.

[20] Y. N. Dastur and W. C. Leslie, “Mechanismof Work Hardening in Hadfield Manganese Steel.,” Metallurgical transactions. A, Physical metallurgy and materials science, Vol. 12 A, No. 5, pp. 749–759, 1981.

[21] E. Mazancová and K. Mazanec, “Stacking fault energy in high manganese alloys,” Materials Engineering, Vol. 16, No. 2, pp. 26–31, 2009.

[22] D. T. Pierce, J. A. Jiménez, J. Bentley, D. Raabe, C. Oskay and J. E. Wittig, “The influence of manganese content on the stacking fault and austenite/ε-martensite interfacial energies in Fe-Mn-(Al-Si) steels investigated by experiment and theory,” Acta Materialia, Vol. 68, pp. 238–253, 2014.